PHOTONICS Research

Silicon-based optical phased array with a reconfigurable aperture for "gaze" scanning of LiDAR

Heming Hu,[1] Yafang He,[1] Baisong Chen,[1] Ziming Wang,[1] Yingzhi Li,[1] Qijie Xie,[2] Quanxin Na,[2] Zihao Zhi,[1] Xuetong Li,[1] Huan Qu,[1] Patrick Lo,[3] and Junfeng Song[1,2,*]

[1]State Key Laboratory of Integrated Optoelectronics, College of Electronic Science and Engineering, Jilin University, Changchun 130012, China
[2]Peng Cheng Laboratory, Shenzhen 518000, China
[3]Advance Micro Foundry Pte. Ltd., Singapore 117685, Singapore
*Corresponding author: songjf@jlu.edu.cn

Received 11 December 2023; revised 14 February 2024; accepted 7 March 2024; posted 7 March 2024 (Doc. ID 515496); published 1 May 2024

Light detection and ranging (LiDAR) serves as one of the key components in the fields of autonomous driving, surveying mapping, and environment detection. Conventionally, dense points clouds are pursued by LiDAR systems to provide high-definition 3D images. However, the LiDAR is typically used to produce abundant yet redundant data for scanning the homogeneous background of scenes, resulting in power waste and excessive processing time. Hence, it is highly desirable for a LiDAR system to "gaze" at the target of interest by dense scanning and rough sparse scans on the uninteresting areas. Here, we propose a LiDAR structure based on an optical phased array (OPA) with reconfigurable apertures to achieve such a gaze scanning function. By virtue of the cascaded optical switch integrated on the OPA chip, a 64-, 128-, 192-, or 256-channel antenna can be selected discretionarily to construct an aperture with variable size. The corresponding divergence angles for the far-field beam are 0.32°, 0.15°, 0.10°, and 0.08°, respectively. The reconfigurable-aperture OPA enables the LiDAR system to perform rough scans via the large beam spots prior to fine scans of the target by using the tiny beam spots. In this way, the OPA-based LiDAR can perform the "gaze" function and achieve full-range scanning efficiently. The scanning time and power consumption can be reduced by 1/4 while precise details of the target are maintained. Finally, we embed the OPA into a frequency-modulated continuous-wave (FMCW) system to demonstrate the "gaze" function in beam scanning. Experiment results show that the number of precise scanning points can be reduced by 2/3 yet can obtain the reasonable outline of the target. The reconfigurable-aperture OPA (RA-OPA) can be a promising candidate for the applications of rapid recognition, like car navigation and robot vision.

https://doi.org/10.1364/PRJ.515496

1. INTRODUCTION

Light detection and ranging (LiDAR) technologies have been widely applied in autonomous driving, environment detection, sensing, etc. [1]. In these applications, all solid-state LiDAR systems have been attracting good attention for their compact size and high robustness [2,3]. Therefore, it has been considered as a promising solution for beaming and steering to supersede the bulky traditional mechanical beam steering. In recent years, various non-mechanical beam-steering methods have been proposed, including micro-electro-mechanical system (MEMS) mirrors [4–6], flash LiDAR [7–9], lens-assisted beam steering (LABS) [10–14], liquid crystal [15–17], and optical phased array (OPA) [18,19]. However, some basic limitations emerge while solving the problem of mechanical beam steering. The MEMS mirror suffers from a limited steering speed as well as the potential problem of mechanical fatigue. Flash LiDAR has a short detection range. For LABS, the scanning angles are discrete rather than continuous. Besides, if there is a need to increase the number of scanning points, the scale of the optical switch would need to be increased exponentially. Currently, OPA-based steering has attracted increasing attention for its advantage of compact size, low power consumption, low cost, and compatibility [20] with standard CMOS processes; it can be expected for the on-chip optoelectronic hybrid LiDAR system in the future [21]. Based on the above reasons, various OPA devices have been explored with different features and merits [22,23], including the power optimization in phase shifters [24,25], the enhancement of grating emission energy

[26,27], the increasement of main lobe power [28,29], and the design of transceiver systems [30].

The angular resolution stands as a crucial parameter for OPA devices. A high angular resolution is constructive to accurate detection of a target object. An effective way to improve resolution of OPA is by reducing the divergence angle. Theoretically, a small divergence angle can be achieved by increasing the effective aperture. Currently, there are typically two approaches to enlarge the effective aperture of the OPA. One method is to increase the quantity of antennas within the OPA. Currently, the state-of-the-art OPA chips can provide up to 8192 available channels [30–32]. However, as the number of channels increases, the complexity of system control grows proportionately. It imposes stringent demands on the OPA control circuit, since precise calibration voltages need to be applied to all channels for beam steering. Besides, as the number of OPA channels increases, the power consumption grows exponentially. It would degrade the stability and life-span of the overall system. The other method to increase the effective aperture is by utilizing an OPA with non-uniform antenna pitch [33,34]. By employing a non-uniform antenna pitch distribution, the effective aperture of the OPA can be greatly increased, resulting in a smaller divergence angle and a wider field of view. However, a portion of the main lobe power and grating lobe power is allocated to side lobes, leading to signals being overwhelmed by the noise-like side lobe during long-distance detection [33]. In addition, blindly increasing the aperture size will lead to an increase in its far-field distance [33,35–37]. Targets within the distance forming the far-field beam cannot be effectively detected, resulting in a blind zone in the field of view. Besides, for the OPAs used in LiDAR applications, not all targets within the field of view are of interest. Hence, much of the distance information in the scanning area is redundant. It can be anticipated that utilizing high resolution to scan across all areas uniformly would result in increased detection complexity, reduced scanning rate, and higher power consumption.

The issues mentioned above can be addressed through adaptive control of the OPA's aperture. Specifically, the aperture size can be determined flexibly according to the desired detection range, scanning precision, and scanning frame rate. In particular, a small aperture is applied in the case of close-range detection for a wide field of view, while a large aperture is used in long-range detection with high transmit-receive power and beam precision. So far, most reported OPAs can only provide fixed divergence angles at the given apertures. Although there are examples of using optical switches to select transmitting antennas [38,39], the purpose is to splice the scanning range in the longitudinal direction by altering the period of the grating, which does not essentially change the aperture size of the OPA.

In this work, we have demonstrated a novel LiDAR structure based on an OPA with reconfigurable apertures. By virtue of the cascaded optical switch, 64-channel, 128-channel, 192-channel, and 256-channel antenna apertures can be switched readily. The corresponding beam divergence angles of OPA can be 0.32°, 0.15°, 0.10°, and 0.08°, respectively. By switching apertures, the far-field distance of the OPA can be changed. This capability helps mitigate the impact of far-field distance on close-range detection and shorten the blind zone, simultaneously. Furthermore, the reconfigurable aperture of the optical phased array is proposed to achieve the gaze scanning function of LiDAR. The function is to perform an initial rough scan of the full field using a small aperture, followed by a fine scan of the target using a larger aperture. Through this approach, both rough scanning with full-range coverage and fine scanning of specific targets can be obtained. Moreover, this approach substantially reduces scanning power consumption and beam steering time. Finally, the reconfigurable aperture OPA is embedded into an FMCW system. To explore the impact of aperture variations on the LiDAR system, a target 2 m away is detected across different apertures. Experiment shows that apertures on one OPA detecting the same target will not distort the distance information. Through this system, we have demonstrated the gaze function in actual scanning. Experiment results indicate that the needed number of fine scanning points can be reduced by 2/3 to obtain the complete outline of the target.

2. STRUCTURE AND CHARACTERISTICS

The designed chip is manufactured in AMF. Figure 1(a) shows the optical microscope image of the fabricated reconfigurable-aperture OPA (RA-OPA). The chip includes a mode size converter, a 1 × 4 optical switch, cascaded Y splitters, a thermo-optical phase shifter, and an aperture group. The silicon waveguide and the silicon-nitride waveguide are designed with sizes of 0.5 μm × 0.22 μm and 1.0 μm × 0.34 μm to support TE mode operation near 1550 nm. Two waveguides are interconnected between layers through adiabatic interlayer transitions. Two loop waveguides are symmetrically placed on the left and right sides of the mode size converter for alignment during OPA packaging. The 1 × 4 optical switch (OSW) is realized via a binary tree of cascaded 1 × 2 Mach–Zehnder interferometer switches. The phase of both the optical switch and the phase

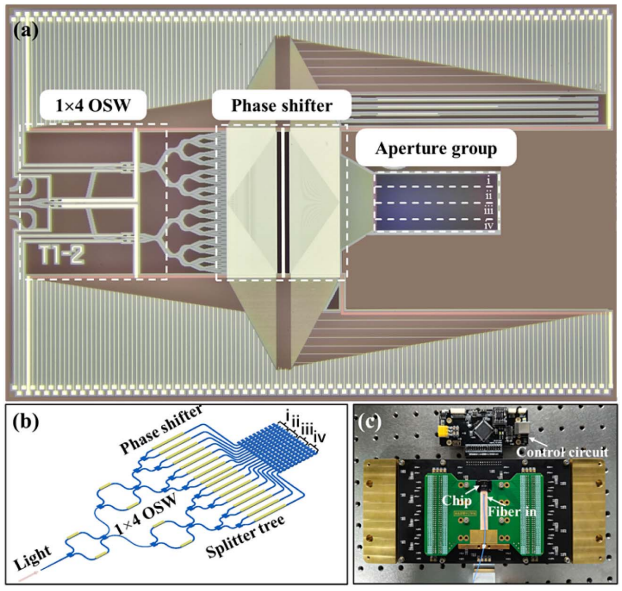

Fig. 1. (a) Optical microscope image of the variable aperture OPA. (b) Schematic of the variable aperture OPA. (c) Electrically and optically packaged variable aperture OPA chip with control circuit.

shifter can be altered via the TiN heater above the waveguide. For a full 2π phase change, two TiN heaters 75 μm long are used in parallel for phase modulation. The maximum static power consumption of the phase shifter is about 15.3 mW. The heat is localized in the waveguide through the undercut process. This method can effectively improve the modulation efficiency of the OPA. Compared with thermal phase shifters that do not use the undercut process, its power consumption is effectively reduced by 75%. A six-level optical beam splitter is connected to each output of the optical switch. Therefore, the original 256-channel grating antenna is evenly divided into four sub-apertures.

As shown in Fig. 1(a), the aperture group consists of four parts as sub-apertures. Each sub-aperture receives signal through the output channel of the optical switch. As shown in Fig. 1(b), the OPA antenna array is divided into four groups labeled by i, ii, iii, and iv. Each group of antennas contains 64 channels, which are eventually combined being a 256-channel large-scale aperture. The antenna pitch is 4 μm and thus the summed aperture of the whole OPA is 1.02 mm. The design of the grating antenna follows the previous work [27]. The fish-bone grating antenna with high emission efficiency is formed through an upper and lower double-layer etching process. The grating has a period L_{period} of 1 μm. The upward emission efficiency of the grating can reach 80%, and the steering efficiency of the grating in the range of 1500–1600 nm is 0.07 deg/nm. Figure 1(b) shows a schematic diagram of the OPA structure. The optical signal is coupled from the external laser into the waveguide through the mode size converter. By controlling the splitting ratio of the output channels within each optical switch, the optical signals can be allocated in any desired proportion and individually directed to a specified cascade beam splitter. The optical signals are phase-modulated by the phase shifters and then directed to the grating antenna array to form a far-field beam. Depending on the power distribution of the optical switch, the OPA can achieve aperture variations from 0.256 to 1.024 mm. Based on the above design, the total insertion loss of this OPA is 10.3 dB, of which the coupling loss from fiber to waveguide is 2.5 dB/facet, the waveguide transmission loss is 1.6 dB/cm, the loss of 1 × 2 MMI is 0.15 dB/junction, the insertion loss of each optical switch is 0.6 dB, and the emission loss of the grating antenna is 2.6 dB. Figure 1(c) shows the electrical and optical package of the chip. The chip is die-attached to the printed circuit board (PCB) and wire-bonded to the pad. The standard single mode fiber is UV-glued on the chip to realize optical signal transmission from laser to chip.

The optical switch embedded in the OPA chip consists of a 1 × 2 beam splitter, two phase modulation arms, and a 2 × 2 beam combiner. The power distribution of the optical switch can be controlled by altering the phase difference between two outputs. The power ratios of the two outputs are both 1/2 when the optical phases are identical to each other. In contrast, all the optical power is emitted only from the one output when the phase difference between the two arms is π. By adjusting the phase difference between the arms, any splitting ratio between zero and one can be obtained from the channels. Based on the above analysis of the optical switch, aperture allocation can be performed as depicted in Fig. 2.

As shown in Fig. 2(a), to ensure the light directed to an output of the OSW2, control voltages are applied to the OSW1 and OSW2 simultaneously, Consequently, there is no light put into OSW3, so its operational state can be disregarded. Under this optical path configuration, only one sub-aperture of the OPA can receive the optical signal and the 64-channel grating antenna array within the aperture serves as the light transmission. As shown in Fig. 2(b), when further increasing the transmitting aperture to a 128-channel grating antenna array, only the phase in OSW2 needs to be adjusted to eliminate the phase difference between the two phase shifters. In this operational state, the optical signals are distributed to output equally, ensuring that two adjacent cascaded beam splitters receive equal optical power. Ultimately, this forms the OPA with a 128-channel grating as the transmitting aperture. Furthermore, as the aperture of the OPA needs to be expanded to 192 channels, the phases of OSW1 and OSW3 are adjusted to distribute the light into three cascaded splitters evenly. The optical path distribution, as shown in Fig. 2(c), depicts a 2/3 connection ratio from OSW1 to OSW2 and a 1/3 connection ratio from OSW1 to OSW3. For OSW3, all the light needs to be output through the channel adjacent to OSW2's output channel. Finally, in order to utilize all channels within the OPA for maximum aperture output, uniform optical intensity needs to be achieved across all splitters. By controlling the phase shifters in OSW1, OSW2, and OSW3 simultaneously, we can eliminate

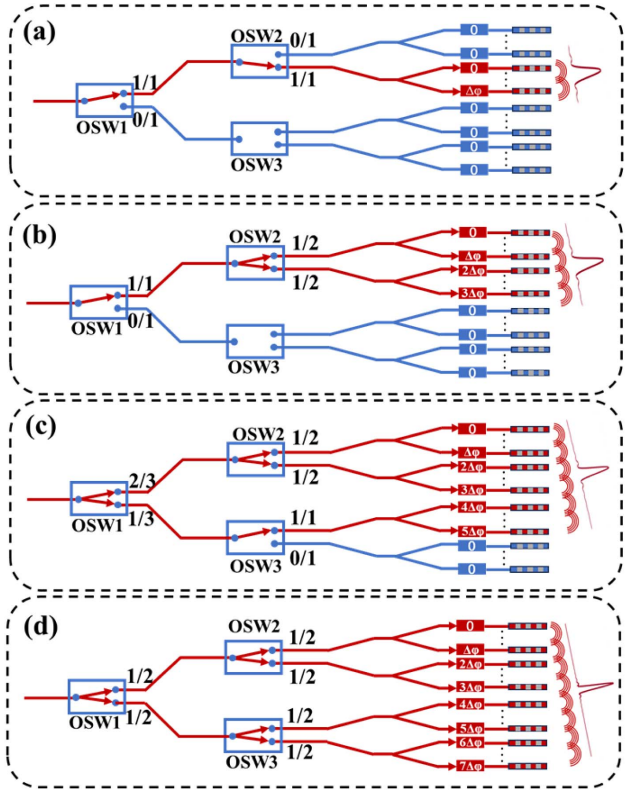

Fig. 2. Schematic diagram of optical path distribution for OPA with (a) 64, (b) 128, (c) 192, and (d) 256 antennas.

the phase differences in these three optical switches. The light signals are split equally among the four output channels, enabling the OPA's 256 channels to function as a single aperture to maximize antenna scalability.

After selecting the required aperture through the optical switch, linear phase modulation is applied to the opened channel. Different sub-apertures will form an overall aperture and generate a far-field interference spot due to linear phase distribution. As shown in Fig. 2, when more channels are turned on, the aperture size will increase, and the corresponding divergence angle will decrease, resulting in a higher resolution of an OPA. The fewer the open channels, the fewer waveguides required to modulate the phase, and the simpler the system.

3. EXPERIMENT RESULTS

A. Characterization of the OPA Chip

The far-field beam formations at 0°, ±5°, and ±10° in the cases of different apertures are tested. The beam steering performances of 64, 128, 192, and 256 channels are shown in Figs. 3(a)–3(d) row by row.

The light spot and cross-sectional curve of the main lobe along θ direction are obtained at a distance of 3 m. The overall lateral FOV of OPA is 22.8°. For OPA, the divergence angle is related to the aperture by [18]

$$\theta_{0.5} \approx \frac{0.88\lambda}{\cos\theta_s N d}\,(\mathrm{rad}), \tag{1}$$

where $\theta_{0.5}$ is the FWHM of the beam, λ is the input light wavelength, θ_s is the scanning angle, N is the number of antennas, and d is the antenna spacing. The FWHM for the scale of 64, 128, 192, and 256 channels is about 0.330°, 0.152°, 0.105°, and 0.083° at a wavelength of 1550 nm. To demonstrate the divergence angle quality of the beam, the measured and simulated divergence angles at 0° are shown in Fig. 4. Note that the actual beam divergence angle closely matches the simulation results, indicating alignment between the aperture and the ideal design.

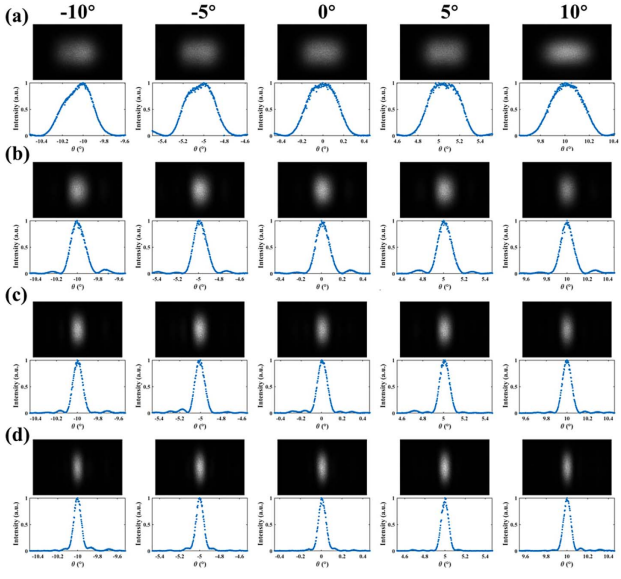

Fig. 3. Beam steering performance of (a) 64, (b) 128, (c) 192, and (d) 256 channels at 0°, ±5°, and ±10°; each contains a light spot picture captured by a near-infrared camera and intensity distribution along the cross section of the light spot.

Beam steering requires precise assignment of phase to each channel, which needs independent voltage control of phase shifters above the waveguides. By reading the voltage and resistance of channels, the actual power consumption of each channel can be calculated, and the overall power consumption of the OPA chip will be obtained by accumulating it. Through this method, the OPA power consumption under different apertures is analyzed in detail. As shown in Fig. 5, the power consumption required for beam steering under different apertures is calculated, and the average power consumption required under each aperture is analyzed. The power consumption with various angles is measured at a wavelength of 1550 nm, where the lateral scanning angle is from −10° to 10°, with an interval of 0.1°. It can be seen from Fig. 5(a) that due to the random phase error that occurs during the processing process, the energy consumption shows a certain degree of randomness for different angles. As shown from Fig. 5(b), the average power consumption of 64 channels, 128 channels, 192 channels, and 256 channels is 243 mW, 486 mW, 720 mW, and 960 mW, respectively. The average power consumption per waveguide is ∼3.8 mW. Through data fitting, the average consumption shows a very good linear relationship with the increment of the waveguide.

In addition, the retarding time for turning on all operation channels is critical for agile beam steering. In our work, we evaluate the required time for turning on the last channel of the 64-, 128-, 192-, and 256-channel OPAs. The measured results of the 64th channel, the 128th channel, the 192nd channel, and the 256th channel are shown in Figs. 6(a), 6(b), 6(c), and 6(d), respectively. It illustrates that the large-channel-scale OPA requires a longer waiting time. This results in an increase in the overall time to configure voltages across all channels as the channel count rises. This incremental time slows down the OPA beam steering rate and thus the frame rate of the LiDAR system.

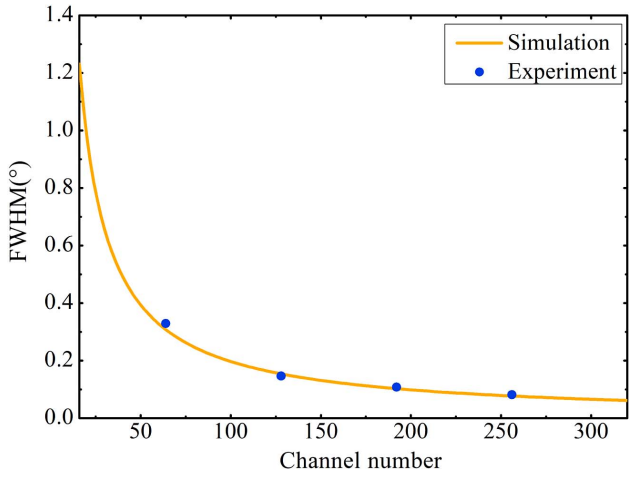

Fig. 4. Main lobe divergence at 0° with different aperture scales.

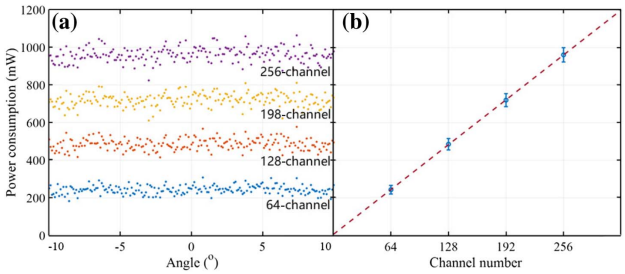

Fig. 5. (a) Power consumption required for steering under different apertures within the range of −10° to 10°; (b) average power consumption under different apertures.

B. Far-Field Distance of the OPA Chip

The far-field distance is crucial to the minimum detection distance. For a typical far-field condition to be satisfied, the distance of the observation needs to meet the following condition [35]:

$$D > \frac{2A^2}{\lambda}, \tag{2}$$

where D is the beam propagation distance, A represents the aperture size of the OPA, and λ stands for the operating wavelength. The increased aperture size extends the far-field distance and thus broadens the scanning blind zone.

In this work, we propose an OPA with a reconfigurable aperture to avoid the blind zone effectively. Figure 7 shows the required propagation distance for the side lobe suppression ratio to reach −10 dB under different aperture sizes. Since the large aperture has a long far-field distance, it cannot effectively perform close-range detection. Therefore, by flexibly switching to a small aperture, the far-field distance can be effectively shortened and its impact on detection can be reduced.

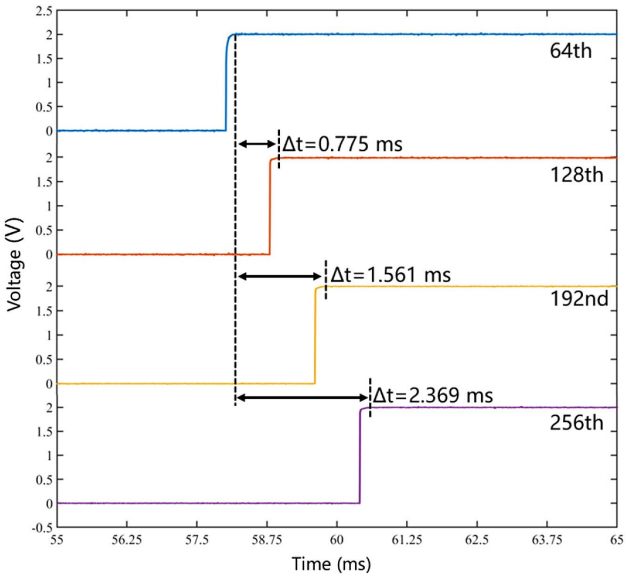

Fig. 6. Configuring the voltage for (a) 64, (b) 128, (c) 192, and (d) 256 channels at the same time, and the turn-on time of the last channel.

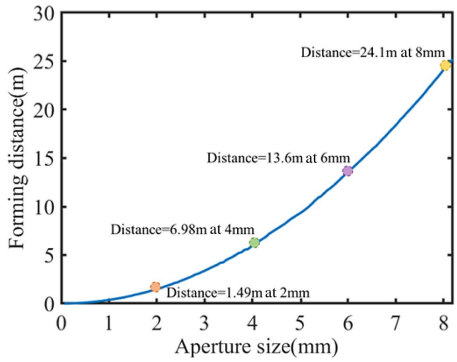

Fig. 7. Far-field distance for different apertures.

To analyze this issue, simulation and experiment are systematically applied under different apertures. Figure 8(a) describes the formation process of the main lobe with distance under different aperture sizes. Figure 8(b) shows the actual spot pattern measured by a near-infrared camera at different distances and different apertures. It shows that as the number of antennas grows, the length of beamforming becomes notably longer. For further analysis, the beam spots formed at three representative distances, [i] 3 cm, [ii] 10 cm, and [iii] 20 cm, are compared. As illustrated by the row [i] in Fig. 8(b), only the 64-channel aperture shows a clear main lobe, while the 128-channel, 192-channel, and 256-channel apertures have not yet reached the far-field distance. Hence, multiple peaks are generated at the position of the main lobe. In particular, six different intensity spots appear in the case of the 256-channel aperture, mainly resulting from the long beamforming distance. As the detection distance increases to 10 cm, the 128-channel aperture also exhibits a distinct main lobe. Meanwhile, although the 192-channel aperture shows the main lobe as well, undesired side lobes are also observed. The beam pattern may cause interference in detection due to strong side lobe power at this distance. In addition, for the 256-channel aperture, the number of light spots is reduced, indicating a trend toward main lobe formation. Finally, as the detection distance reaches 20 cm, distinct main lobes for all apertures are well observed. As shown in the row [iii] of Fig. 8(b), the light spots of the 64 channels, 128 channels, and 192 channels further compress and exhibit normal beam quality under this distance. Hence, by selecting appropriate emission apertures for different distances, significant reduction in the blind zone can enhance the detection performance of the OPA.

C. Gaze Scanning Function Enabled by the RA-OPA

High points density leads to accurate restoration of an actual scene. The resolution of a point cloud is closely related to the aperture size of OPA. However, most reported OPAs are designed with fixed apertures, so their resolution and scanning frequency frame rate are fixed at the time of manufacture. Besides, high-density point cloud scanning is often power and time consuming. Hence, rich scanning details normally compromise scanning frame rate. By physically altering the aperture size of OPA, the LiDAR "gaze" scanning function balances scanning points and frame rates. As illustrated in Fig. 9, in the "gaze" mode, OPA with a small aperture is used to scan

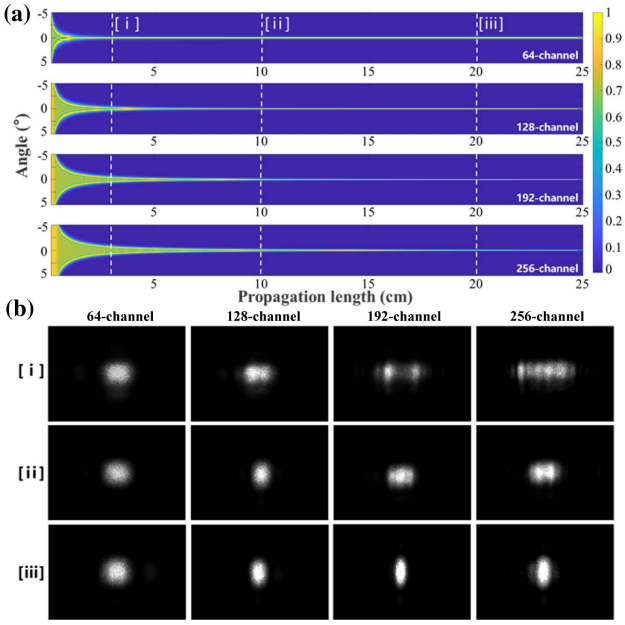

Fig. 8. (a) Simulated formation process for light beams of 64-, 128-, 192-, and 256-channel OPA along with distance; (b) captured beam spot at the distance of 3 cm, 10 cm, and 20 cm.

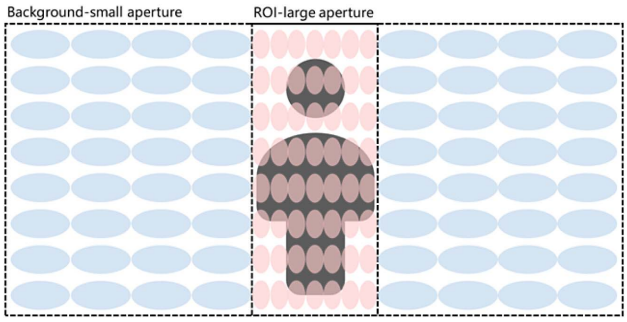

Fig. 9. Schematic diagram of gaze scanning using different apertures.

the frontal area with sparse scanning points, while the large aperture is used to enhance the point cloud resolution, so that richer details in the ROI can be perceived. This methodology resembles the way that the human eye "gazes" at an object. It ensures the OPA point cloud frame rate while also considering the details within the ROI.

To introduce the gaze function, 64-channel and 256-channel apertures are used for demonstration. As shown in Figs. 10(a) and 10(b), the measured far-field patterns of 64-channel and 256-channel apertures over 20° are exhibited, respectively.

Since the divergence angle of the 64-channel aperture is four times that of the 256-channel aperture, the 64-channel and 256-channel apertures are scanned at steps of 0.8° and 0.2°, respectively. Light points are displayed in the θ direction spanning from −10° to 10°. To change the angle of the light points in the φ direction, we modify the wavelength from 1520 to

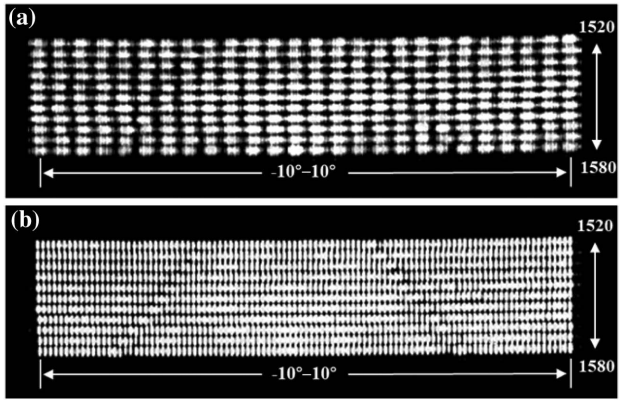

Fig. 10. Sum of the normalized far-field spot obtained by the (a) 64-channel aperture and (b) 256-channel aperture steering with laser wavelength and phase shift.

1580 nm in 6 nm increments. Covering the entire scanning area requires 311 scan points for the 64-channel aperture, while the 256-channel aperture demands an increase to 1212 scan points. Hence, the number of point clouds required can be reduced by a 64-channel aperture, while a high-precision scanning can be obtained within range by an aperture of 256 channels.

The performance of the RA-OPA is tested with gaze scanning. Figure 11(a) displays a picture of the scanned letters "JLU." As depicted in Fig. 11(b), a rough scan of the JLU letters was achieved by switching to the 64-channel aperture. The rough position of the letters can be perceived. It can be found that only one to two detected points are observed on each letter. Then, without changing the background scanning resolution, the three letters "JLU" are accurately scanned by the same OPA chip switched to the 256-channel aperture. As shown

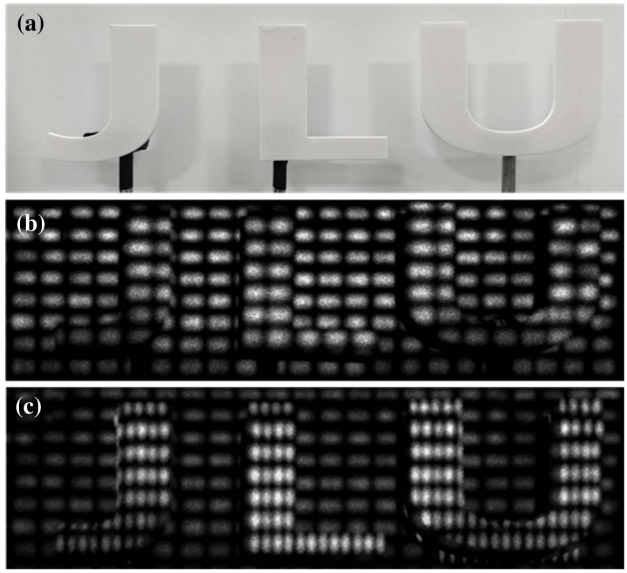

Fig. 11. (a) Picture of the letters JLU as a scanning target; (b) full-range scanning using 64-channel aperture; (c) gaze on the letters J, L, and U using 256-channel aperture.

in Fig. 11(c), J, L, and U are gazed at by the 256-channel aperture. The details of each letter can be detected and the number of detectable points on each letter is also increased by four times. Based on the gaze scanning function, only 149 points are contained within the letters of J, L, and U. It is far fewer than the points required for fine scanning with the large aperture. Hence, this unique scanning method allows RA-OPA to better focus on critical targets at a physical level.

D. RA-OPA Embedded FMCW LiDAR Ranging

By using the proposed OPA, a frequency-modulated continuous-wave (FMCW) ranging system is demonstrated. The schematic of FMCW LiDAR circuit is illustrated in Fig. 12. The OPA is added to the system as a transmitter (TX) and a beam collimator is added as a receiver (RX) in the system. A single wavelength laser is modulated by the single sideband (SSB) modulator to generate a modulated triangular optical signal. The modulation bandwidth is 3 GHz. The modulated signal is amplified by the erbium-doped fiber amplifier (EDFA). The amplified light is distributed into a local oscillator (LO) signal and TX signal at a ratio of 0.1:0.9. The TX signal is coupled into the OPA for scanning. The reflected light is received through a collimator and coherently beaten against the LO. A balanced detector containing a transimpedance amplifier (TIA) converts the light signal into voltage signal, and the multichannel high-speed analog-to-digital converter (ADC) reads the voltage signal, which can be analyzed by digital signal processing (DSP). The generated beat frequency is proportional to the target distance. The target distance is given by $D = fc/2\alpha$, where f is the beat frequency, c is light speed, and α is frequency sweep rate. In addition, the distance D consists of fiber optical length and target distance.

The ranging uniformity of OPA with different apertures is measured. The experimental setup is depicted in Fig. 13(a). Figures 13(b)–13(e) illustrate RF spectra for beat signals in the cases of OPA with 64-channel, 128-channel, 192-channel, and 256-channel apertures. The steering angle is 0° and the distance is 2 m. As can be seen from the figure, using different apertures on one OPA to detect the same distance target will not distort the distance information. The peak frequencies detected across all apertures are 2.083 MHz. However, the signal-to-noise pedestal ratios (SNPRs) vary under different apertures. The SNPRs for 64-channel, 128-channel, 192-channle, and 256-channle apertures are ∼14 dB, ∼16 dB, ∼21 dB, and

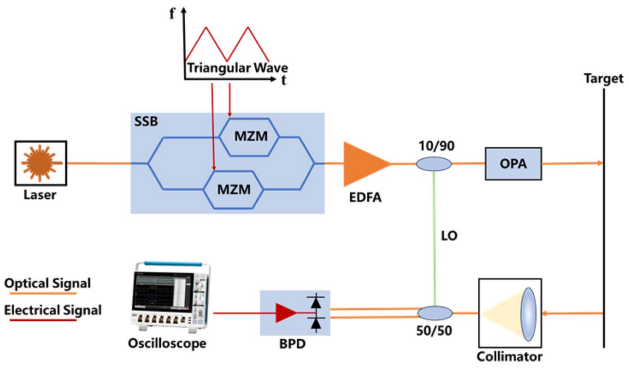

Fig. 12. Schematic diagram of RA-OPA embedded FMCW LiDAR system.

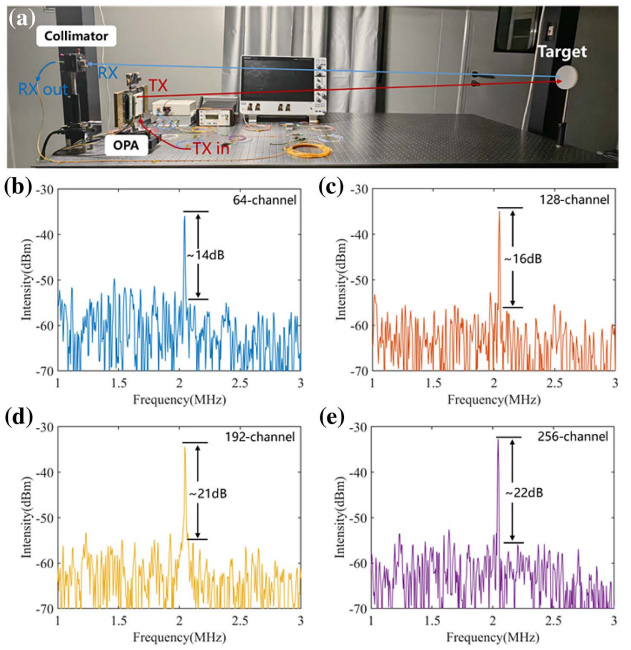

Fig. 13. (a) Picture of experimental setup. RF spectra for the beat signal in the cases of (b) 64-channel, (c) 128-channel, (d) 192-channel, and (e) 256-channel OPA at a distance of 2 m.

∼22 dB. The SNPR differences across apertures are primarily due to the divergence in θ. As the aperture increases, the divergence angle of the beam decreases, resulting in a more concentrated signal power at the target position. Therefore, the signal power obtained at the same position is significantly higher than that of the noise, thereby enhancing the signal resolution.

To demonstrate the gaze function of RA-OPA, a one-dimensional object scanning was conducted. In the following measurements, three targets are placed at distances of 1.7 m from the OPA, as shown in Fig. 14(a). The length of each side of the square is 20 cm, the vertex angle of the isosceles triangle is 30°, and the side length is 20 cm. The upper base of the isosceles trapezoid is 10 cm, and the lower base is 30 cm. The side lengths of the left and right sides are 20 cm, and the angle between the upper base and the side is 120°. The gap between the three objects is 10 cm.

Three scanning methods are used on the object. Figure 14(b) shows a rough scan using the OPA with a 64-channel aperture at a step of 1° to capture the basic outline of the objects. This scan clearly shows surface outlines including the front of the square, edges of the trapezoid, and the background. However, due to the larger scanning angle, details at the corners and the triangle could not be detected. Under this scanning, only 27 points are required. Similarly, a precise scanning of a three-project outline is shown. Figure 14(c) shows the precise outline of the object captured through 256 apertures in a step of 0.2°. In this scanning method, all details of the object can be obtained, including the vertices of triangles, the two vertex angles of trapezoids, etc. However, the higher resolution causes wasted detail for the square's front and background. The number of points required for this precise scan is 269, significantly

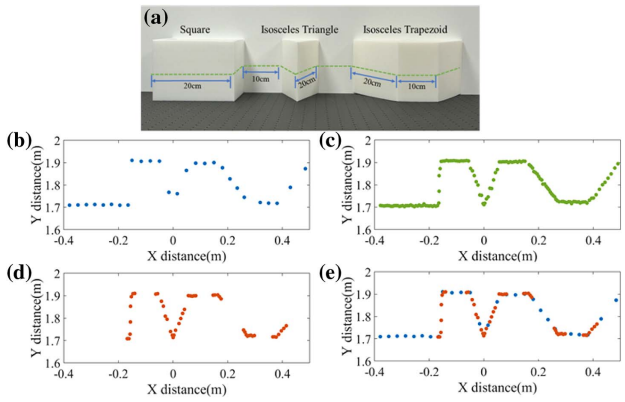

Fig. 14. (a) Picture of targets placed in front of the OPA in different directions; (b) experimental result for a rough scan of the target by using 64-channel aperture; (c) experimental result for a fine scan of the target by using 256-channel aperture; (d) gaze at the corner of the target using 256-channel aperture; and (e) target position information obtained by splicing rough scan and gaze areas.

increasing the scanning complexity. This problem can be addressed by using a gaze function. As shown in Fig. 14(d), details missed by the rough scan can now be detected by focusing on the corner positions of the target objects. Finally, by splicing all the data from both the rough and gazed scans, a one-dimensional profile of the object comparable to a high-precision scan is obtained in Fig. 14(e). Based on this method, only 80 points are needed, with 27 from rough scanning and 57 from fine scanning—just one-third of the points needed for the high-resolution scan. This method greatly reduces the scanning time and complexity.

4. CONCLUSION

In conclusion, we have demonstrated an OPA with a reconfigurable aperture from 64 to 256 channels. Attributed to the 1×4 optical switch, 64-channel, 128-channel, 192-channel, and 256-channel antenna apertures can be readily switched. Based on the aperture transformations, the beam divergence angle of OPA can be 0.32°, 0.15°, 0.10°, and 0.08°. By switching the aperture, the far-field distance of the OPA can be minimized. The OPA enables close-range beam scanning, significantly reducing the blind spots of the OPA. Meanwhile, the gaze function is proposed through the reconfigurable aperture. By switching the aperture of OPA, it is possible to achieve a broad-range rough scan and fine scanning of individual targets. This capability enables the OPA to reduce scanning time while ensuring accurate capture of object details. Finally, the OPA is embedded into a frequency-modulated continuous-wave (FMCW) system to discuss the impact of aperture changes on detecting and demonstrate the gaze function in actual scanning. Experiments indicate that the needed number of fine scanning points can be reduced by 2/3 to obtain the outline of the target. This demonstrates that reconfigurable aperture OPA is a promising candidate for transmitting and receiving optical signals in LiDAR systems.

For the current microwave photonic radar, it can already realize the function of detecting and tracking multiple targets with a single aperture [40–42]. However, the developed OPA-based LiDAR is still at the stage of single target detection. This is mainly limited by the fact that OPA LiDAR uses a single light source and an overall controlled phase modulation system. Although silicon photonic chips are easy for on-chip integration, multiple independent OPA chips can be integrated on one chip with independent light sources and phase control, and ultimately achieve the purpose of focusing on multiple targets at the same time. However, multi-target scanning with OPA under a single aperture is still a very challenging task needing further study.

Funding. Program for Jilin University Science and Technology Innovative Research Team (2021TD-39); Jilin Provincial Development and Reform Commission Project (2020C056); Major Scientific and Technological Program of Jilin Province (20210301014GX); National Natural Science Foundation of China (62105173, 62105174, 61934003, 62090054); National Key Research and Development Program of China (2022YFB2804504).

Disclosures. The authors declare no conflicts of interest.

Data Availability. Data underlying the results presented in this paper are not publicly available at this time but may be obtained from the authors upon reasonable request.

REFERENCES

1. M. J. R. Heck, "Highly integrated optical phased arrays: photonic integrated circuits for optical beam shaping and beam steering," Nanophotonics **6**, 93–107 (2017).
2. M. X. Hu, Y. Pang, and L. Gao, "Advances in silicon-based integrated LiDAR," Sensors **23**, 5920 (2023).
3. N. X. Li, C. P. Ho, J. Xue, *et al.*, "A progress review on solid-state LiDAR and nanophotonics-based LiDAR sensors," Laser Photonics Rev. **16**, 2100511 (2022).
4. O. Solgaard, A. A. Godil, R. T. Howe, *et al.*, "Optical MEMS: from micromirrors to complex systems," J. Microelectromech. Syst. **23**, 517–538 (2014).
5. J. Rodriguez, B. Smith, B. Hellman, *et al.*, "Multi-beam and single-chip LIDAR with discrete beam steering by digital micromirror device," Proc. SPIE **10526**, 105260U (2018).
6. C. Errando-Herranz, N. L. Thomas, K. B. Gylfason, *et al.*, "Low-power optical beam steering by microelectromechanical waveguide gratings," Opt. Lett. **44**, 855–858 (2019).
7. Q. Hao, Y. Tao, J. Cao, *et al.*, "Development of pulsed-laser three-dimensional imaging flash lidar using APD arrays," Microw. Opt. Technol. Lett. **63**, 2492–2509 (2021).
8. F. Villa, F. Severini, F. Madonini, *et al.*, "SPADs and SiPMs arrays for long-range high-speed light detection and ranging (LiDAR)," Sensors **21**, 3839 (2021).
9. P. F. McManamon, P. Banks, J. Beck, *et al.*, "Comparison of flash LiDAR detector options," Opt. Eng. **56**, 031223 (2017).
10. Z. Y. Zhang, B. Chen, Q. Zhang, *et al.*, "A fully solid-state beam scanner for FMCW LiDAR application," IEEE Photonics Technol. Lett. **35**, 377–380 (2023).
11. X. Y. Cao, G. Qiu, K. Wu, *et al.*, "LiDAR system based on lens assisted integrated beam steering," Opt. Lett. **45**, 5816–5819 (2020).
12. C. Li, X. Cao, K. Wu, *et al.*, "Lens-based integrated 2D beam-steering device with defocusing approach and broadband pulse operation for LiDAR application," Opt. Express **27**, 32970–32983 (2019).
13. C. Li, X. Cao, K. Wu, *et al.*, "Blind zone-suppressed hybrid beam steering for solid-state LiDAR," Photonics Res. **9**, 1871–1880 (2021).

14. C. Rogers, A. Y. Piggott, D. J. Thomson, *et al.*, "A universal 3D imaging sensor on a silicon photonics platform," Nature **590**, 256–261 (2021).
15. J. Beeckman, K. Neyts, and P. J. M. Vanbrabant, "Liquid-crystal photonic applications," Opt. Eng. **50**, 081202 (2011).
16. R. Morris, C. Jones, and M. Nagaraj, "Liquid crystal devices for beam steering applications," Micromachines **12**, 247 (2021).
17. J. Kolacz, H. G. Gotjen, R. Y. Bekele, *et al.*, "Propagating transverse electric and transverse magnetic modes in liquid crystal-clad planar waveguides," Liq. Cryst. **47**, 531–539 (2020).
18. C. P. Hsu, B. Li, B. Solano-Rivas, *et al.*, "A review and perspective on optical phased array for automotive LiDAR," IEEE J. Sel. Top. Quantum Electron. **27**, 8300416 (2021).
19. S. Zhao, J. Chen, and Y. Shi, "All-solid-state beam steering via integrated optical phased array technology," Micromachines **13**, 894 (2022).
20. H. Q. Qiu, Y. Liu, X. Meng, *et al.*, "Energy-efficient integrated silicon optical phased array," Front. Optoelectron. **16**, 23 (2023).
21. W. H. Xu, Y. Guo, X. Li, *et al.*, "Fully integrated solid-state LiDAR transmitter on a multi-layer silicon-nitride-on-silicon photonic platform," J. Lightwave Technol. **41**, 832–840 (2023).
22. Z. H. Zhi, Q. Na, Q. Xie, *et al.*, "On-chip generation of Bessel-Gaussian beam via concentrically distributed grating arrays for long-range sensing," Light Sci. Appl. **12**, 92 (2023).
23. Y. Z. Li, B. Chen, Q. Na, *et al.*, "High-data-rate and wide-steering-range optical wireless communication via nonuniform-space optical phased array," J. Lightwave Technol. **41**, 4933–4940 (2023).
24. S. P. Liu, J. Feng, Y. Tian, *et al.*, "Thermo-optic phase shifters based on silicon-on-insulator platform: state-of-the-art and a review," Front. Optoelectron. **15**, 9 (2022).
25. S. A. Miller, Y.-C. Chang, C. T. Phare, *et al.*, "Large-scale optical phased array using a low-power multi-pass silicon photonic platform," Optica **7**, 3–6 (2020).
26. Y. Q. Shuai, Z. Zhou, and H. Su, "Toward practical optical phased arrays through grating antenna engineering," Photonics **10**, 520 (2023).
27. B. S. Chen, Y. Li, L. Zhang, *et al.*, "Unidirectional large-scale waveguide grating with uniform radiation for optical phased array," Opt. Express **29**, 20995–21010 (2021).
28. H. Q. Qiu, Y. Liu, X. Meng, *et al.*, "Bidirectional high sidelobe suppression silicon optical phased array," Photonics Res. **11**, 659–668 (2023).
29. L. X. Zhang, Y. Li, B. Chen, *et al.*, "Two-dimensional multi-layered SiN-on-SOI optical phased array with wide-scanning and long-distance ranging," Opt. Express **30**, 5008–5018 (2022).
30. C. V. Poulton, M. J. Byrd, P. Russo, *et al.*, "Coherent LiDAR with an 8,192-element optical phased array and driving laser," IEEE J. Sel. Top. Quantum Electron. **28**, 8300416 (2022).
31. C. M. Sun, B. Li, W. Shi, *et al.*, "Large-scale and broadband silicon nitride optical phased arrays," IEEE J. Sel. Top. Quantum Electron. **28**, 8200710 (2022).
32. G. Z. Luo, L. Yu, P. Ma, *et al.*, "A large-scale passive optical phase array with 1024 channels," IEEE Photonics Technol. Lett. **35**, 927–930 (2023).
33. Y. Z. Li, B. Chen, Q. Na, *et al.*, "Wide-steering-angle high-resolution optical phased array," Photonics Res. **9**, 2511–2518 (2021).
34. D. W. Zhuang, L. Zhang, X. Han, *et al.*, "Omnidirectional beam steering using aperiodic optical phased array with high error margin," Opt. Express **26**, 19154–19170 (2018).
35. D. Kwong, A. Hosseini, Y. Zhang, *et al.*, "1 × 12 Unequally spaced waveguide array for actively tuned optical phased array on a silicon nanomembrane," Appl. Phys. Lett. **99**, 051104 (2011).
36. A. Hosseini, D. Kwong, Y. Zhang, *et al.*, "Modeling and experimental observation of an on-chip two-dimensional far-field interference pattern," Appl. Opt. **50**, 1822–1826 (2011).
37. W. H. Xu, C. Liu, Y. Guo, *et al.*, "Impact of aperture size on beam evolution of optical phased arrays," in *Optical Fiber Communications Conference and Exhibition (OFC)* (2021), pp. 1–3.
38. Z. Y. Zhou, Z. Zhang, Q. Huang, *et al.*, "Multi-line selective optical phased array with improved uniformity of radiated beam patterns," IEEE Photonics Technol. Lett. **34**, 133–136 (2022).
39. L. X. Zhang, Y.-Z. Li, M. Tao, *et al.*, "Large-scale integrated multi-lines optical phased array chip," IEEE Photonics J. **12**, 6601208 (2020).
40. S. S. S. Panda, T. Panigrahi, S. R. Parne, *et al.*, "Recent advances and future directions of microwave photonic radars: a review," IEEE Sens. J. **21**, 21144–21158 (2021).
41. F. Z. Zhang, B. Gao, and S. Pan, "Photonics-based MIMO radar with high-resolution and fast detection capability," Opt. Express **26**, 17529–17540 (2018).
42. X. P. Liu and K. Wang, "Research on high-resolution wide-swath SAR based on microwave photonics," in *CIE International Conference on Radar (RADAR)* (2016), pp. 1–3.